Liu *et al. Microstructures* 2024;4:2024024
DOI: 10.20517/microstructures.2023.65

Microstructures

Research Article

Open Access

Check for updates

Hot isostatic pressing induced precipitation strengthening at room and high temperature of Ni-Fe-Cr-Al-V high-entropy alloy manufactured by laser powder bed fusion

Ziwei Liu[1], Zhen Tan[1], Zheng Zhou[1], Wei Shao[1], Xingye Guo[1], Dingyong He[1,2], Li Cui[1], Yunfei Xue[3], Lixia Ma[1]

[1]College of Materials Science and Engineering, Beijing University of Technology, Beijing 100124, China.
[2]Beijing Engineering Research Center of Eco-Materials and LCA, Beijing 100124, China.
[3]School of Materials Science and Engineering, Beijing Institute of Technology, Beijing 100081, China.

Correspondence to: Prof. Lixia Ma, College of Materials Science and Engineering, 100 Pingleyuan Street, Chaoyang District, Beijing 100124, China. E-mail: maxia@bjut.edu.cn; Prof. Zhen Tan, College of Materials Science and Engineering, 100 Pingleyuan Street, Chaoyang District, Beijing 100124, China. E-mail: zhen.tan@bjut.edu.cn

How to cite this article: Liu Z, Tan Z, Zhou Z, Shao W, Guo X, He D, Cui L, Xue Y, Ma L. Hot isostatic pressing induced precipitation strengthening at room and high temperature of Ni-Fe-Cr-Al-V high-entropy alloy manufactured by laser powder bed fusion. *Microstructures* 2024;4:2024024. https://dx.doi.org/10.20517/microstructures.2023.65

Received: 28 Oct 2023 **First Decision:** 28 Nov 2023 **Revised:** 26 Dec 2023 **Accepted:** 2 Feb 2024 **Published:** 25 Apr 2024

Academic Editor: Huijun Li **Copy Editor:** Fangling Lan **Production Editor:** Fangling Lan

Abstract

The highly adjustable properties of high-entropy alloys (HEAs) offer great potential for developing superior materials for critical structural applications in high-temperature conditions. In this study, Ni-Fe-Cr-Al-V HEA was manufactured by laser powder bed fusion, which has a unique microstructure composed of dislocation substructure and Face-centered cubic + $L1_2$ coherent structure and achieves the desired strength-ductility combination. Hot isostatic pressing post-treatment was applied on the laser powder bed fusion-processed HEA to further improve the relative density and optimize the mechanical properties. During the hot isostatic pressing process, the precipitation of $L1_2$ and B2 phases can be ascribed to the precipitation modes dominated by continuous precipitation and discontinuous precipitation, respectively. With the tensile deformation temperature increasing from 773-1,173 K, the softening degree of HEA increases continuously, and the dominant deformation mechanism evolves from intragranular dislocation slip to grain boundary sliding. At temperatures below 773 K, precipitation strengthening significantly improves tensile strength and ductility. At 1,173 K, the grain boundary strength decreases and grain boundary area increases, which promotes grain boundary sliding and contributes to plastic deformation, resulting in significant softening.

Keywords: Laser powder bed fusion, high-entropy alloy, hot isostatic pressing, precipitation strengthening, mechanical property

INTRODUCTION

As a major breakthrough in the field of materials, high-entropy alloys (HEAs) were initially defined as alloys containing more than five principal elements with the atomic concentration of each between 5% and 35%[1,2]. HEAs exhibit a simple solid solution phase due to their larger configuration entropy than most metallics materials[3]. The combination of sluggish diffusion, severe lattice distortion, high entropy, short-range ordering and cocktail effects leads to their excellent performance, such as the high strength at ambient[4], cryogenic[5] and high temperatures[6] and high corrosion resistance[7], oxidation[8], and fatigue[9].

In particular, high-temperature structural parts are one of the most promising applications for HEAs, because lattice distortion and sluggish diffusion can lead to solid solution strengthening, which, in turn, contributes to improving high-temperature properties[10]. Therefore, HEAs have more high-temperature application potential than Ni-based superalloys. Refractory HEAs (RHEAs) have shown remarkable specific strength at temperatures up to 1,473 K, exceeding that of Ni-based superalloys[11], while their ductility remains low and cannot meet the needs of practical applications. There is an urgent need to produce a balanced combination of HEAs with excellent high-temperature strength, reasonable room-temperature ductility, and good environmental resistance. The HEAs composed of γ (Face-centered cubic, FCC) and γ′ ($L1_2$) phases have a similar microstructure to Ni-based superalloys, and the yield strength (YS) is observed to increase anomalously with increasing temperature[12]. When exposed to 923 K, the $Al_5Ti_5Co_{35}Ni_{35}Fe_{20}$ HEA presented the highest mechanical properties, which was caused by γ′ precipitates[13].

Laser powder bed fusion (LPBF) exhibits great potential for preparing HEAs owing to its high cooling and solidification rates and large geometric design freedom[14]. LPBF technology is a widely applied additive manufacturing (AM) approach that employs a laser to selectively melt successive metal powder layers in a chamber filled with inert gas[15]. It has been reported that HEAs prepared through LPBF processes have superior room-temperature mechanical properties than those produced using conventional methods[16,17]. These superior properties are ascribed to the presence of specific microstructural features at different length scales, especially the fine cellular substructures[18]. Annealing studies have revealed that these cellular substructures may be stable at 873 K[19] and disappear after annealing at 1,173 K[20]. This high stability of the substructures at relatively high temperatures contributes to delaying the tensile fracture of LPBF-processed HEAs during high-temperature tensile testing, thereby obtaining excellent high-temperature mechanical properties.

Hot isostatic pressing (HIP) is a common post-processing technology that simultaneously uses high temperature and pressure to reduce defects, optimize microstructure, and enhance high-temperature properties[21-23]. It was reported that the defect volume fraction of the LPBF-processed Ni-based superalloy was reduced from 0.96% to 0.08% after the HIP process[21]. Moreover, the high temperature used in HIP treatment can facilitate precipitation strengthening, change the columnar morphology of the grains, and weaken the crystallographic texture. The formation of equiaxed grains of LPBF-processed Inconel 718 alloy after HIP mitigates the mechanical anisotropy at both room and high temperatures[24]. Thus, HIP is also considered as a promising approach to improve the high-temperature properties of LPBF-processed HEAs.

In this study, a non-equiatomic heterostructured Ni-Fe-Cr-Al-V HEA was developed. The composition is designed to facilitate the phase separation to achieve a near-equiatomic FCC matrix *in situ*, alongside forming high content $L1_2$ phases, which includes ~50 at. % Ni concentration, ~4 Ni/Al ratio, and ~4 at. % V can stabilize and strengthen $L1_2$ phases[25,26]. The Ni-Fe-Cr-Al-V alloy prepared by LPBF has an "FCC + $L1_2$"

microstructure, which has been proven to contribute to excellent strength and ductility at room temperature[17]. In order to improve the oxidation resistance required for high-temperature applications, the addition of Al, Ni and Cr to HEAs has been attempted, which is indeed favorable for the oxidation resistance at high temperatures[27]. The cellular substructures commonly formed in LPBF-processed alloys exhibit high stability above 873 K[28], effectively improving the strength and ductility[29,30]. Thus, the Ni-Fe-Cr-Al-V HEA is expected to achieve excellent high-temperature properties, and HIP was adopted to further improve its high-temperature characteristics. The relationship between microstructure and high-temperature properties in LPBF-processed HEA has not been mentioned or investigated thoroughly in other studies. Therefore, Ni-Fe-Cr-Al-V HEAs were produced by LPBF technology and HIP post-treatment, and their microstructure evolution, room-temperature and high-temperature tensile properties, and deformation mechanism were investigated, respectively. The obtained results can be used to establish the relationship between processing, microstructure and property of HEAs and provide guidance for subsequent processing.

MATERIALS AND METHODS

Material preparation

Gas-atomized Ni-Fe-Cr-Al-V HEA powder was used for LPBF preparation. The Scanning electron microscopy (SEM) image of the powder shows the morphology with a notable sphericity containing few satellites [Figure 1A]. Figure 1B demonstrates the particle size distribution analyzed using a Tod laser particle analyzer, and the average particle size is 31.6 μm. The chemical composition of powder was measured via an X-ray Fluorescence Spectrometer (XRF, Panalytical Axiosmax), as listed in Table 1.

An LPBF machine, EOS M100, with a 200 W fiber laser source, was employed to prepare samples. The process was performed under argon atmosphere with the concentration of O_2 controlled below 10 ppm. The laser rotation angle between any adjacent layers was 67°. The optimum process parameters (laser powder = 130 W, laser scanning speed = 800 mm/s, layer thickness = 0.02 mm, hatch spacing = 0.05 mm) were adopted. The samples were removed from 316L stainless steel substrate using electrical discharge machining.

After the LPBF process, the HIP post-treatment was conducted on a RD200/300-2000-200 HIP furnace under an argon atmosphere, followed by furnace cooling. The heating rate of the HIP was 293 K/min. Based on our previous studies, the defects within the LPBF-processed Ni-Fe-Cr-Al-V HEA could be eliminated effectively upon HIP treatment at 1,573 K and 150 MPa for 4 h[31]. Hence, the same HIP parameters were applied in this study to eliminate defects in the LPBF-processed HEA.

Microstructural characterization

The vertical section planes of the cubic samples were ground and polished in accordance with the standard procedures for metallographic examinations. The densities of LPBF-processed and HIP-processed HEAs were measured by a drainage method based on Archimedes principle, as determined by[32]

$$\rho = \frac{M_{dry}}{(M_{dry} - M_{Arch})/\rho_w} \quad (1)$$

where M_{dry} is the weight of the dried samples, M_{Arch} is the weight of the buoyancy samples in distilled water, and ρ_w is the density of distilled water at 298 K, i.e., 0.99707 g/cm^3. The results for each alloy were calculated by averaging three measurements to verify accuracy. The densities of LPBF-processed and HIP-processed HEAs were measured to be 7.885 and 7.891 g/cm^3, respectively. The theoretical density was calculated to be

Table 1. Chemical composition of the Ni-Fe-Cr-Al-V powder

Element	Ni	Fe	Cr	Al	V
wt. %	51.26	20.95	17.36	6.44	3.85
at. %	46.10	19.76	17.59	12.57	3.98

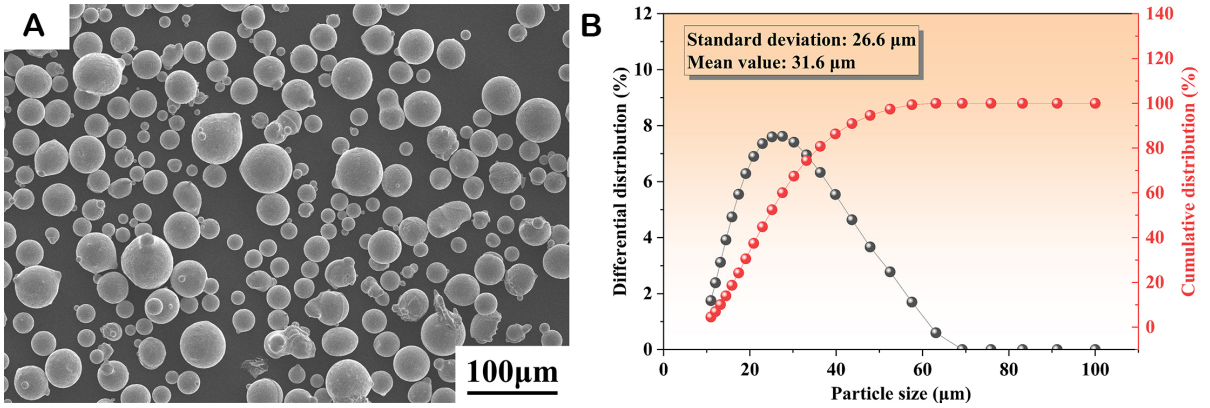

Figure 1. (A) Powder morphology and (B) particle size distribution.

7.895 g/cm^3. The relative densities obtained from dividing the actual density by the theoretical density are 99.87% and 99.94%, respectively. The difference in relative density is related to the quantification of internal defects. Furthermore, the relative densities were also quantified using Image J software[33]. Five 1 mm × 1 mm areas were randomly selected in each SEM image to calculate the relative density. The phase composition was examined by X-ray diffraction (XRD, D8 Advance) with Cu Kα radiation at 40 kV and 20 mA. The samples were mechanically polished and then etched with a Mable solution (20 g $CuSO_4$, 100 mL HCl, 5 mL H_2SO_4 and 80 mL H_2O), and the microstructure was observed using SEM (Quanta 650) in the secondary electron mode. The phase distribution and grain size were determined by electron backscattered diffraction (EBSD) in a step size of 1.5 μm. EBSD data was analyzed using HKL Channel 5 software. The samples were ground to 50 μm, punched into a 3 mm disc using a hole punch, and then thinned by Gatan 691 PIPS for transmission electron microscope (TEM) analysis. Then, a TEM equipped with an energy dispersive spectroscopy (EDS) detector was used for further internal microstructure characterization and chemical analysis.

Tensile testing

The dimensions of the room and high-temperature tensile samples are shown in Figure 2. The dog-bone-shaped tensile samples feature gage dimensions of 34.4 mm × 9.5 mm × 0.9 mm. Tensile tests were conducted at room (293 K) and high temperatures (773 and 1,173 K) on a ZWICK/ROELL-Z050 universal test machine, respectively. The deformation displacement of tensile specimens was recorded using grating rulers (HEIDENHAIN, Germany) and extension poles. A heating rate of 20 K/min and air cooling were applied. The temperature at which the grain boundary strength is equal to grain strength is defined as the equicohesive temperature (ET), usually around 0.5 T_m (T_m is melting point temperature)[34]. The ET of the Ni-Fe-Cr-Al-V HEA was calculated to be ~953 K. Therefore, high-temperature tensile tests were chosen to be performed at temperatures above (1,173 K) and below (773 K) the ET, respectively. The measurement precision of 0.2% offset YS, ultimate tensile strength (UTS) and fracture elongation (FE) were improved by averaging three testing values. Note that the loading direction during tensile testing was perpendicular to the building direction (BD).

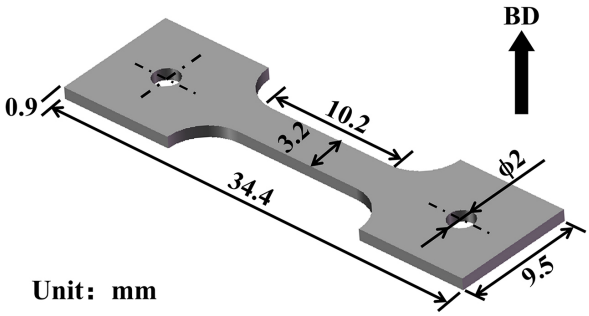

Figure 2. Schematic of the dimensions of tensile samples (building direction referred to as BD).

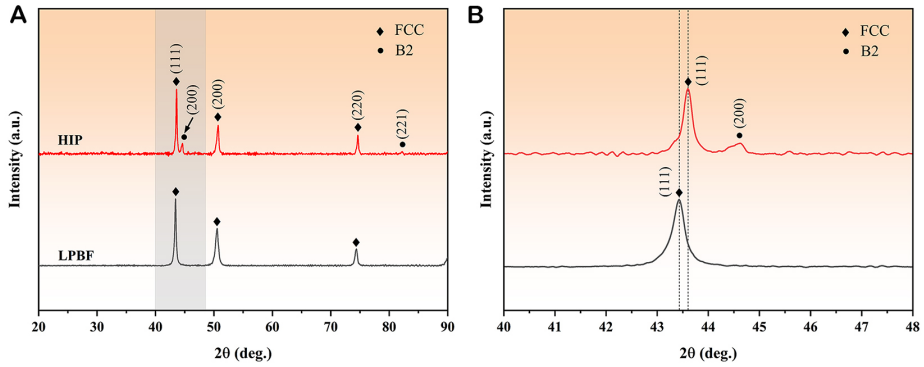

Figure 3. (A) XRD patterns of LPBF-processed and HIP-processed Ni-Fe-Cr-Al-V HEAs and (B) magnified image of the grey region in (A).

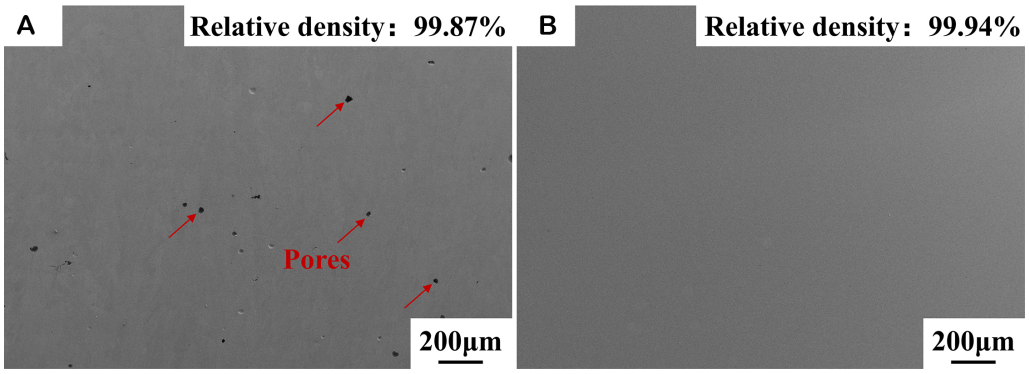

Figure 4. SEM images of the pores in (A) LPBF-processed Ni-Fe-Cr-Al-V HEAs and (B) HIP-processed HEA.

RESULTS

Microstructural evolution

Figure 3 shows the XRD results of as-built and HIP-processed Ni-Fe-Cr-Al-V HEAs. The as-built HEA exhibited a single FCC structure. After HIP treatment, the HEA showed a duplex (FCC + B2) structure. Furthermore, the diffraction peaks of the HIP-processed HEA slightly shift to high diffraction angles, in comparison with that of the as-built HEA, suggesting the decreased lattice parameters [Figure 3B]. According to the Bragg equation and interplanar spacing equation of cubic crystals, the lattice parameters of FCC phases are calculated to be 0.360 and 0.358 nm, respectively. The decreased lattice parameter could be attributed to the precipitation of the B2 phase.

Figure 4 shows the pores in LPBF-processed Ni-Fe-Cr-Al-V HEAs before and after HIP treatment. Relative densities were calculated using Image J software. Some pores could be observed in the as-built HEA, and the relative density was calculated to be 99.87% [Figure 4A]. After HIP treatment, pores were significantly eliminated, and the relative density increased to 99.94% [Figure 4B]. The densities calculated by Archimedes principle and Image J software are consistent.

Figure 5 shows the SEM and EBSD micrographs of the microstructure in as-built HEA. The molten pool boundaries could be found in an as-built sample [Figure 5A]. The typical columnar grains grew across multiple layers along the building direction. There were substructures with different orientations within the grains [Figure 5B]. The inverse pole figure (IPF) map showed the columnar grain morphology, and the average grain width of the columnar grains was calculated to be 19.48 μm according to EBSD analysis [Figure 5C]. The phase distribution map in Figure 5D indicated that the as-built HEA contained a single FCC structure, which was in accordance with the XRD results in Figure 3.

TEM analysis was conducted to thoroughly observe the microstructure of the as-built HEA, as shown in Figure 6. A large number of cellular substructures were widely distributed in the as-built HEA [Figure 6A]. Dense dislocations were trapped inside the substructure. Also, a few nanoparticles were observed in the high-resolution transmission electron microscopy (HRTEM) [Figure 6B]. Based on the HRTEM image of the nanoparticles and corresponding selected area electron diffraction (SAED) patterns, it could be identified that the nanoparticles distributed in the matrix were $L1_2$ phases [Figure 6C and D]. The $L1_2$ phase could not be detected by XRD and SEM results due to its nanoscale size and low volume fraction.

Figure 7 shows the SEM and EBSD micrographs of the microstructure in HIP-processed HEA. Upon HIP treatment, the molten pool tracks disappeared and substructures were annihilated. The grain morphology became irregularly shaped, and the grain size became uneven [Figure 7A]. Furthermore, striped precipitates were observed at the grain boundaries and grain interior [Figure 7B]. The size of the striped precipitate along the grain boundaries was larger than that in the grain interior. It can be inferred that these striped precipitates are B2 phases in conjunction with the XRD results. The average grain width was calculated to be 14.14 μm according to EBSD analysis [Figure 7C]. It could be further confirmed that the striped precipitates were B2 phases based on the phase map in Figure 7D.

Figure 8 presents the TEM micrographs of the HIP-processed HEA. Striped precipitates could be clearly observed along the grain boundaries in Figure 8A. SAED patterns corresponding to the area I indicated the striped precipitates were B2 phases. According to the element distribution maps, the striped phase was enriched in Al and Ni, and a block of Cr-V-rich precipitate was observed within the striped phase [Figure 8B]. Besides, a dark field TEM (DF-TEM) image of the matrix (area II) presented numerous cellular precipitates in ~20 nm in the matrix [Figure 8C]. The corresponding SAED patterns and element distribution maps indicated the Al-Ni rich cellular precipitates were coarsened $L1_2$ phases [Figure 8D].

Mechanical properties

Figure 9 shows the engineering stress-strain curves and corresponding work hardening rate curves of as-built and HIP-processed HEAs at room (293 K) and high temperatures (773 and 1,173 K), respectively, and the detailed tensile properties are presented in Table 2. In terms of the room-temperature tensile curves [Figure 9A], the as-built HEA exhibited UTS of 1,088 MPa and FE of 27.9%. After HIP treatment, there was a significant increase in strength (UTS: 1,334 MPa) and a decrease in ductility (FE: 15.1%). The high-temperature tensile curves at 773 K displayed that the UTS of ~926 MPa and FE of ~23.8% were obtained in the as-built HEA, while the UTS increased significantly to 1,267 MPa and FE decreased slightly to 20.2%

Table 2. Tensile properties of LPBF-processed and HIP-processed Ni-Fe-Cr-Al-V HEAs from room to high temperatures in comparison with Cr-Fe-Ni alloys

Sample	Temperature (K)	Ultimate tensile strength (MPa)	Yield strength (MPa)	Fracture elongation (%)
LPBF-processed Ni-Fe-Cr-Al-V	293	1,088 ± 21	619 ± 17	27.9 ± 0.92
	773	926 ± 16	658 ± 14	23.8 ± 0.72
	1,173	136 ± 15	69 ± 11	17.6 ± 0.69
HIP-processed Ni-Fe-Cr-Al-V	293	1,334 ± 27	807 ± 22	15.1 ± 0.76
	773	1,267 ± 19	882 ± 16	20.2 ± 0. 67
	1,173	113 ± 14	77 ± 10	28.5 ± 0.75
Cr-Fe-Ni[35]	298	~570	~280	~40
	673	~420	~170	~38
	873	~220	~125	~10
	1,073	~155	~130	~2

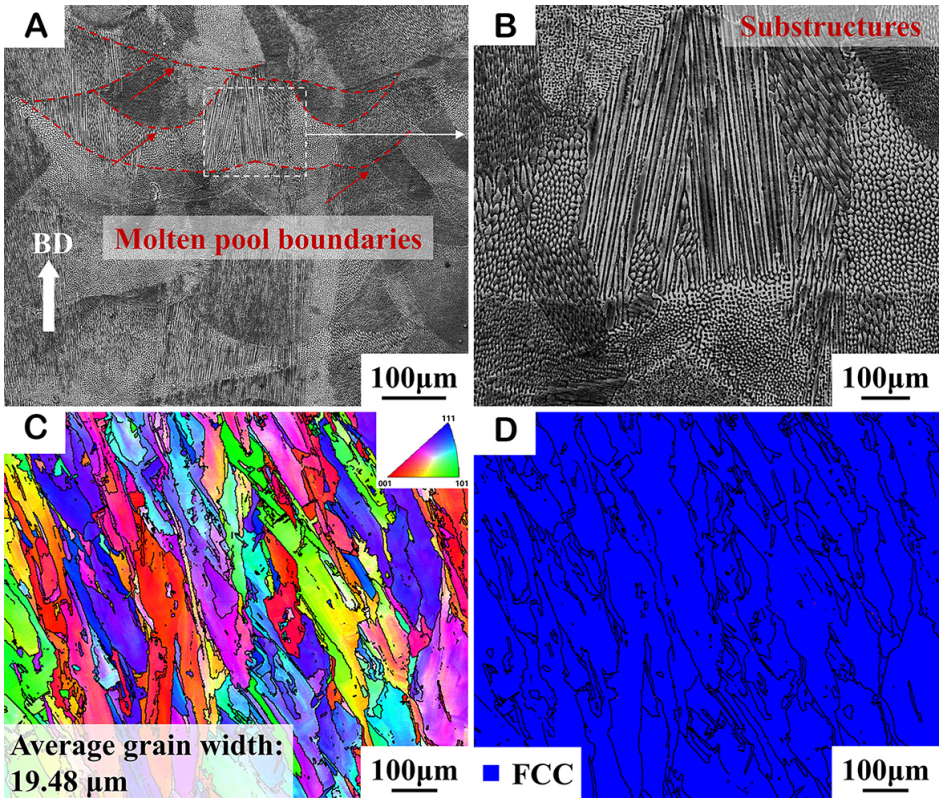

Figure 5. SEM and EBSD micrographs of the microstructure in LPBF-processed Ni-Fe-Cr-Al-V HEA: (A) molten pools, (B) substructures, (C) IPF map and (D) phase distribution map.

after HIP treatment, as shown in Figure 9C. Figure 9E shows the high-temperature tensile curves at 1,173 K. Obviously, both as-built HEA and HIP-processed HEAs exhibited remarkable softening behavior, with lower UTS of about 136 and 113 MPa, respectively. In particular, extremely high and low FEs of about 28.5% and 17.6% were achieved in HIP-processed HEA and as-built HEA specimens, respectively. Compared with the Cr-Fe-Ni medium-entropy alloy[35], the LPBF-processed HEA exhibits superior tensile strength at both room and high temperatures. When tested at 1,173 K, the HEA and Cr-Fe-Ni alloy have comparable tensile strength, but the former has a much higher FE.

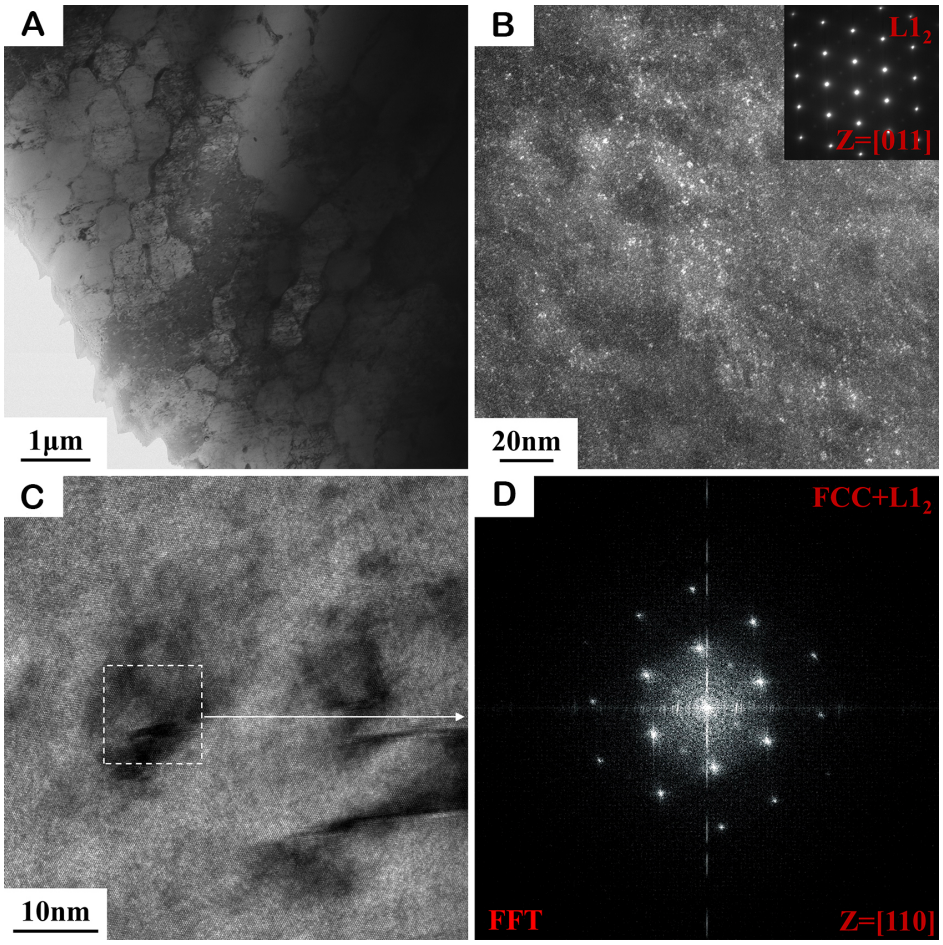

Figure 6. TEM micrographs of the microstructure in LPBF-processed Ni-Fe-Cr-Al-V HEA: (A) Bright field (BF) image of cellular substructures; (B) BF image of nanoparticles in matrix; (C) HRTEM image of nanoparticles; (D) (Fast Fourier transform) FFT patterns of white rectangle region in (C).

The work hardening rate ($d\sigma/d\varepsilon$) curves were plotted according to the true stress-strain curves. At 293 K, the high initial work hardening rates of both as-built and HIP-processed HEAs might be induced by the interaction between the dislocation substructures or between dislocations and precipitates. The work hardening rate curves could be divided into two stages. In stage I ($\varepsilon < 3\%$), the work hardening rate significantly decreased as the true strain increased, which might be related to the dislocation annihilation and rearrangement during deformation. In stage II ($\varepsilon > 3\%$), the work hardening rate remains positive but decreased slowly with increasing deformation, which may be related to the gradual overcoming of slip barriers and deformation being driven by cross-slip[36]. Especially, the HIP-processed HEA always had superior work hardening capability over the as-built HEA during the whole deformation process, which may be mainly caused by the precipitation of B2 phase [Figure 9B]. At 773 K, the work hardening rate of the HIP-processed HEA is higher than that of the as-built HEA, indicating the HIP-processed HEA has better work hardening capability. The work hardening rate is always greater than 0, indicating that the deformation process at 773 K was dominated by hardening [Figure 9D]. In contrast, at 1,173 K, the work hardening rate at the later deformation stage is negative, demonstrating that softening behavior has occurred [Figure 9F]. Compared to the LPBF-processed HEA, the softening behavior occurs later in the HIP-processed HEA with a longer hardening stage, resulting in greater resistance to localized necking, which contributes to the higher FE.

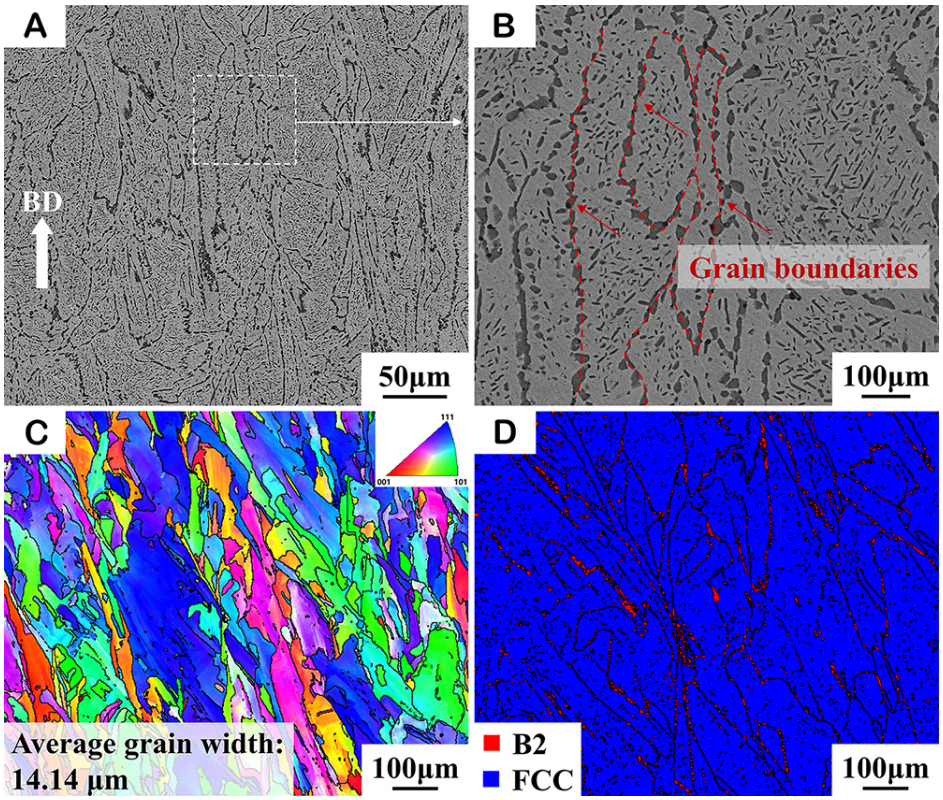

Figure 7. SEM and EBSD micrographs of the microstructure in HIP-processed Ni-Fe-Cr-Al-V HEA: (A and B) grain morphology and B2 phases, IPF map and (C and D) phase distribution map.

Figure 10 shows the fracture morphologies of Ni-Fe-Cr-Al-V HEAs at 293 K. Both fracture morphologies show that the fracture mode is dominated by ductile fracture [Figure 10A and C]. Furthermore, the enlarged images of the red rectangular regions are presented in Figure 10B and D, respectively. Dense dimple structures are observed in both samples, but the dimple size of the LPBF-processed HEA is smaller than that of the HIP-processed HEA, which is consistent with the higher elongation.

The cross-sectional morphology near the fracture tip and the fracture morphology of the HEAs after tensile deformation at 773 K is displayed in Figure 11. It can be observed that the side surface of the fractured specimens tested at 773 K was smooth and flat [Figure 11A and D]. Moreover, no precipitate was observed in LPBF-processed HEA after tensile testing at this temperature, indicating that the thermal-mechanical coupling does not induce the precipitation of B2 phase at 773 K. Many tiny dimples and some prior pores were observed on the fracture surface of the LPBF-processed HEA, as shown in Figure 11B. In addition, many parallel striations were found on the surface of pores [Figure 11C]. Both the dimples and striations indicate that the LPBF-processed HEA has good ductility. Some secondary cracks can be observed on HIP-processed HEA, as displayed in Figure 11E, which may result from stress concentration at the hard B2 phase. In addition, dense and tiny dimples can be seen on both sides of the secondary cracks [Figure 11F], indicating ductile fracture.

Figure 12 presents the fractography of the tensile fracture surface and the microstructure of the cross section near the fracture of HEAs after tensile deformation at 1,173 K. Obviously, a large number of small cracks were on the cross surface [Figure 12A and D] and the majority were distributed along the grain boundaries and propagated along the grain boundaries, which may be related to the stress concentration caused by the

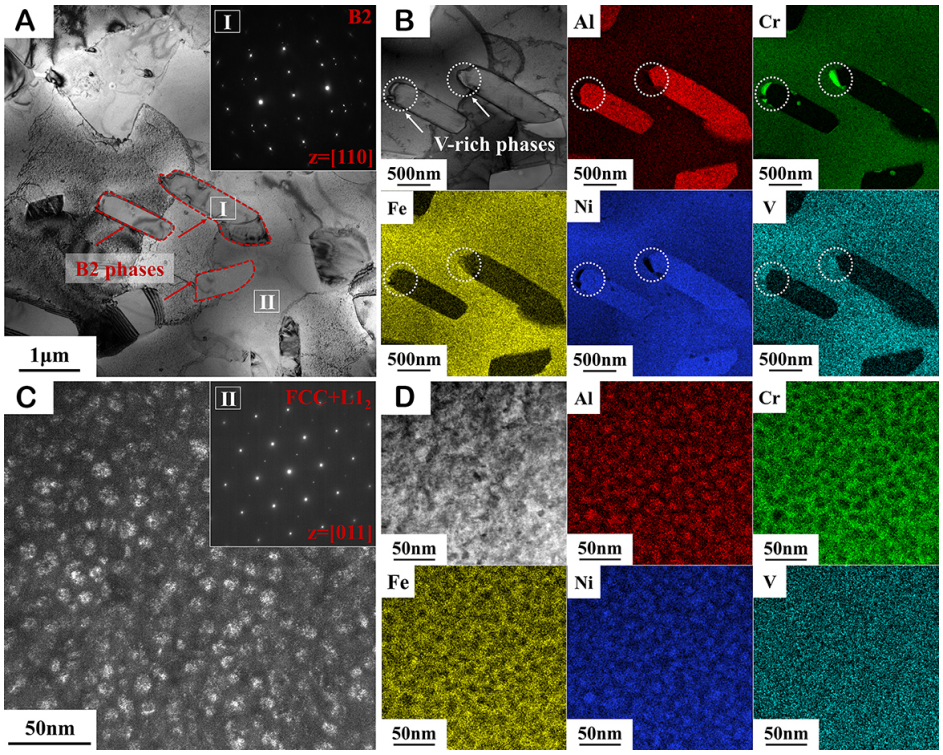

Figure 8. TEM micrographs of the microstructure in HIP-processed Ni-Fe-Cr-Al-V HEA: (A) BF-TEM image and SAED pattern of B2 precipitates, (B) EDS maps of B2 phases, (C) DF-TEM image and SAED pattern of $L1_2$ precipitates and (D) EDS maps of $L1_2$ precipitates.

deformation mismatch between B2 and FCC phases. Additionally, many small cracks will converge at multiple grain boundary intersections to form large cracks, as shown in Figure 12B and E. In addition, large numbers of precipitated phases were discovered at the grain boundaries and the grain interior, indicating that the thermal-mechanical coupling can induce the precipitation of B2 phase during deformation at 1,173 K. Furthermore, no dimples are observed [Figure 12C and F].

DISCUSSION

Microstructural evolution during HIP treatment

During the HIP treatment, alloys were subjected to high temperature and pressure, which acts as a pressurized heat treatment and leads to microstructural change. After HIP treatment, pores were significantly eliminated, and the relative density increased from 99.87% to 99.94%. The pore closure process by HIP can be divided into two stages. Firstly, plastic deformation occurs at high temperatures and pressures, with most of the pores closing, which results in the inner surfaces coming into contact with each other (stage I). Then, the elements diffuse between the closed pore interfaces (stage II). After HIP treatment, sufficient elemental diffusion and good metallurgical bond strength at the pore interface lead to excellent mechanical properties of HEAs[31]. However, the residual internal pores were associated with their trapped argon gas. The high internal pressure within the pores hindered the further closure of the pores. Figure 13 clearly presents the microstructural evolution under LPBF and HIP states. The characteristic microstructure of HEAs prepared by LPBF processes consists of molten pool tracks and substructures, which disappeared completely after HIP treatment. Dislocation substructures are commonly observed in LPBF-processed alloys and may annihilate after heat treatment[37-39]. Actually, the alloy composition at the molten pool/substructure boundary was slightly different from that inside the molten pool/substructure. The HIP treatment promoted atomic diffusion, which led to a homogenization of segregation and the elimination of the molten pool

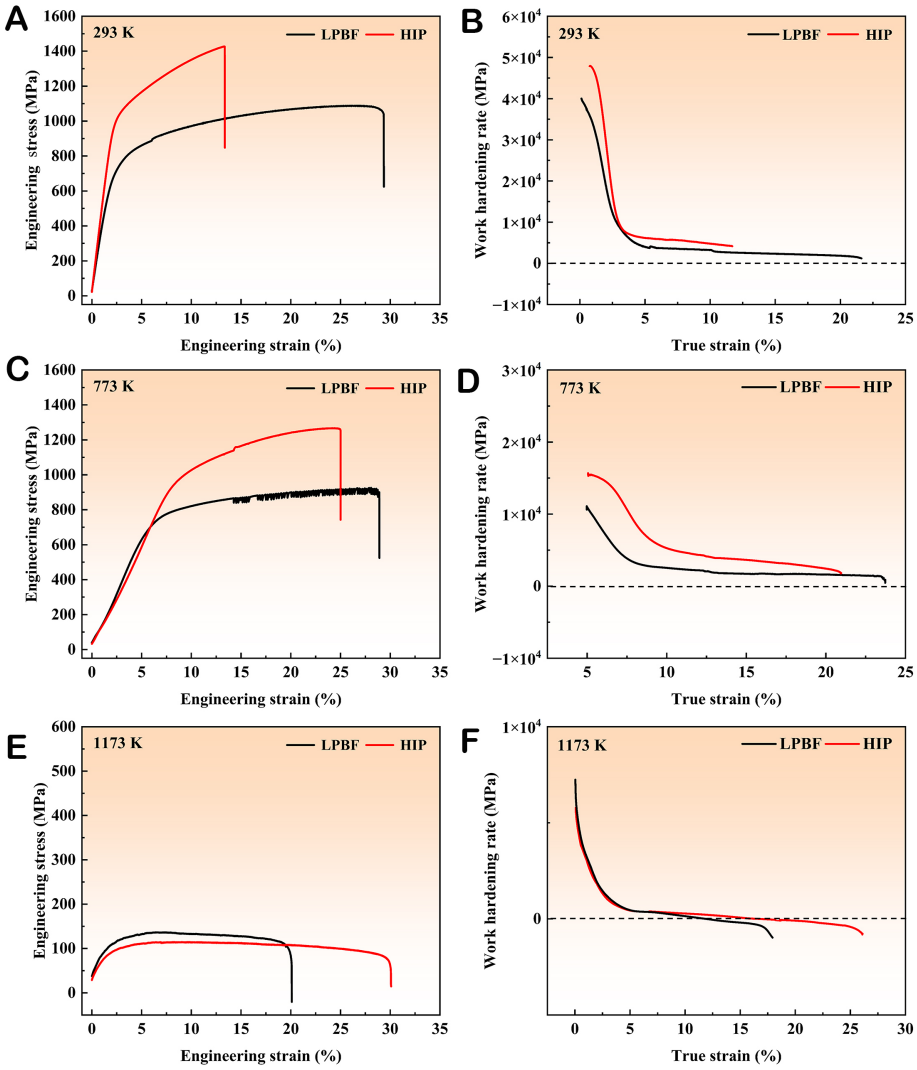

Figure 9. Engineering stress-strain curves and corresponding work hardening rate curves of LPBF-processed and HIP-processed Ni-Fe-Cr-Al-V HEAs tested at (A and B) 293 K, (C and D) 773 K and (E and F) 1,173 K, respectively.

boundaries and substructures[40]. Furthermore, there is no increase in the grain size of HEAs during HIP treatment. When treated at relatively high temperatures, dislocations slip occurred at the cell interior, some dislocations of the opposite sign on the cell walls annihilated, and then gradually transformed into dislocation networks of low energy or sub-grain boundaries. The sub-grain boundaries would further transform into grain boundaries with the decrease of dislocation density within the sub-grains. Additionally, the pinning effect by the B2 phase at grain boundaries also obstructed the grain growth[41].

The LPBF-processed HEA consists of FCC matrix and $L1_2$ nanoparticles with a size of several nanometers. Upon high temperature and pressure, the B2 phases precipitated at grain boundaries and grain interior, while $L1_2$ nanophases grew up to ~20 nm in the FCC matrix. There are two common precipitation modes in precipitation-strengthened alloys, i.e., continuous precipitation (CP) and discontinuous precipitation (DP). The CP means the uniform precipitation within the grains in which the solute concentration is continuously changing in the matrix. On the contrary, the DP usually develops at grain boundaries and enters into the grain interior by alternately lamellated growth of the solute-depleted matrix and precipitates[42]. Based on

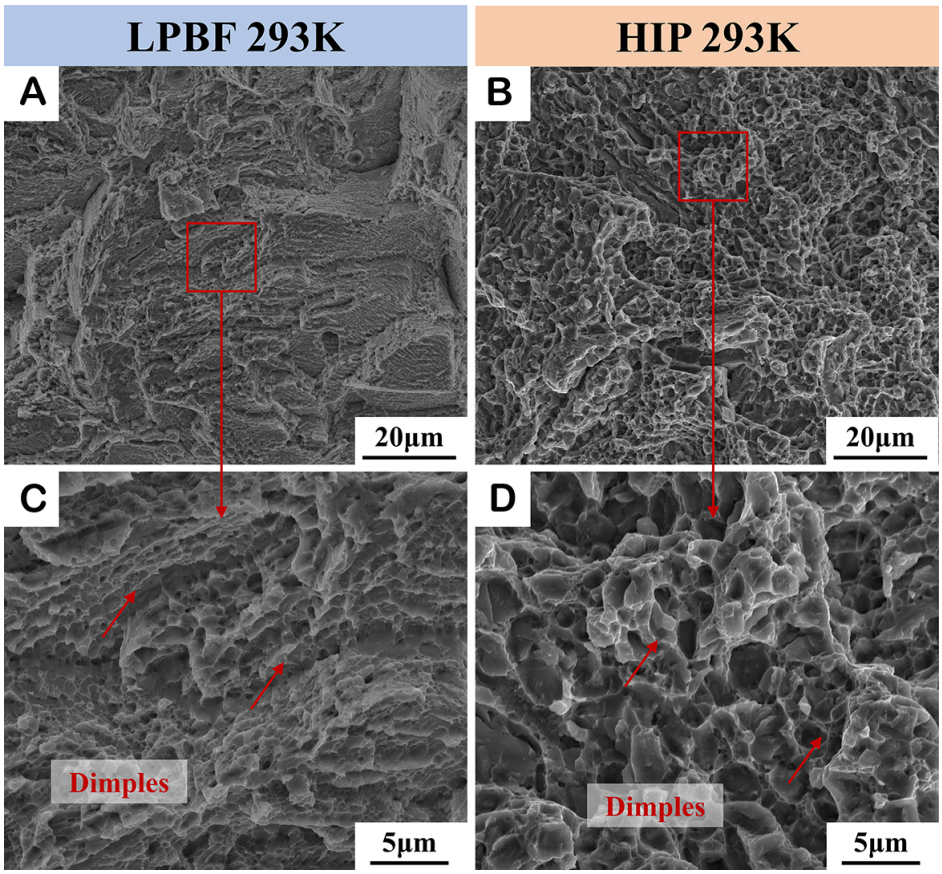

Figure 10. Fracture morphologies of Ni-Fe-Cr-Al-V HEAs at 293 K: (A and B) LPBF-processed and (C and D) HIP-processed.

the uniform distribution of the $L1_2$ phase in the FCC matrix, the growth of the $L1_2$ phase was considered as CP reaction, which could be explained by precipitate nucleation and growth. The reserved residual dislocations after HIP might be favorable for the strength enhancement due to the dislocation strengthening mechanism. In addition, the residual dislocations can provide heterogeneous nucleation sites for the $L1_2$ phases and serve as fast paths for atomic diffusing. The high-density dislocation facilitated the rapid growth of $L1_2$ precipitates. The volume fraction of $L1_2$ nanoparticles in the HIP-processed HEA increased due to the enhancement of nucleation and growth of $L1_2$ precipitates in the matrix. For the precipitation mode of the B2 phase, CP and DP occurred simultaneously during the HIP process. Initially, the DP initiated at grain boundaries and extends to the grain interior via cellular reactions, resulting in the formation of B2 precipitates. Subsequently, the CP became the dominant mode and led to the formation of uniformly distributed B2 precipitates within the grains. Moreover, the accelerated CP reaction will restrict the DP reaction. Based on the thermodynamics analysis, the difference in solute concentration at the migration grain boundary is the driving factor for the DP growth. The rapid nucleation and growth of the CP decreases the supersaturation of the FCC matrix, which, in turn, reduces the solute concentration gradient of the migrating grain boundaries and the driving factor of the DP reaction. The relatively coarse CP nanoparticles can inhibit grain boundary migration and dynamically delay the growth of DP. Thus, the simultaneous occurrence of the two precipitation modes resulted in two different morphologies of the B2 phases, i.e., the coarse size at grain boundaries and the fine size within the grains.

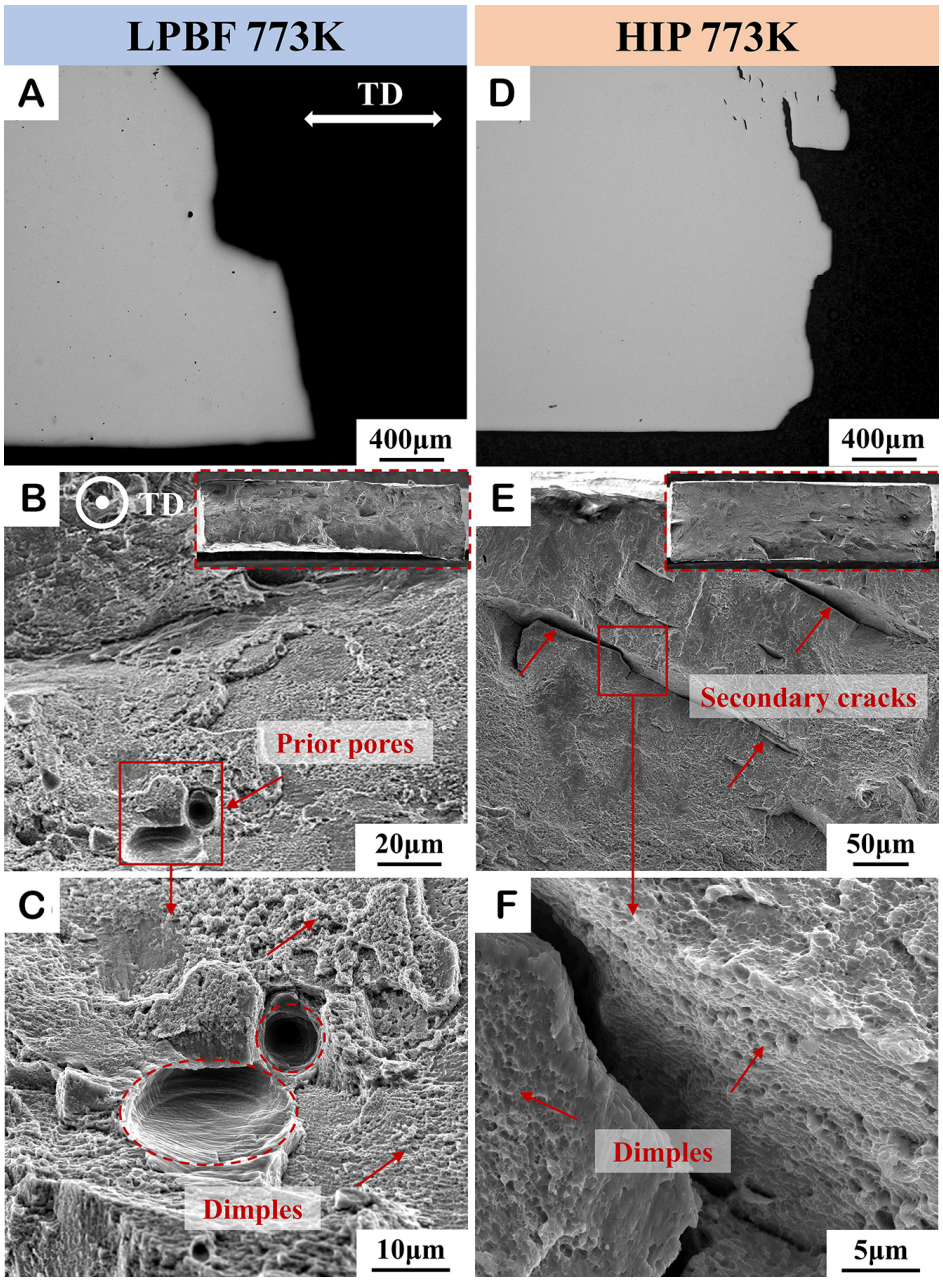

Figure 11. Fracture morphologies of Ni-Fe-Cr-Al-V HEAs at 773 K: (A-C) LPBF-processed and (D-F) HIP-processed.

Deformation mechanism

At room temperature

LPBF-processed alloys can break the strength-ductility mismatch at room temperature, and this combination of high strength and ductility can be attributed to the unique microstructure characteristics, especially cellular substructures. The LPBF-processed Ni-Fe-Cr-Al-V HEA exhibited high strength and good ductility due to the dislocation substructure and coherent $L1_2$ nanophase. The presence of substructure implied a significant increase in dislocation density, resulting in the high strength. During the deformation process, the hindered dislocations are allowed to transmit through the dislocation walls with the increase of stress, enabling the stable plastic flow. In addition, the misorientation between substructures

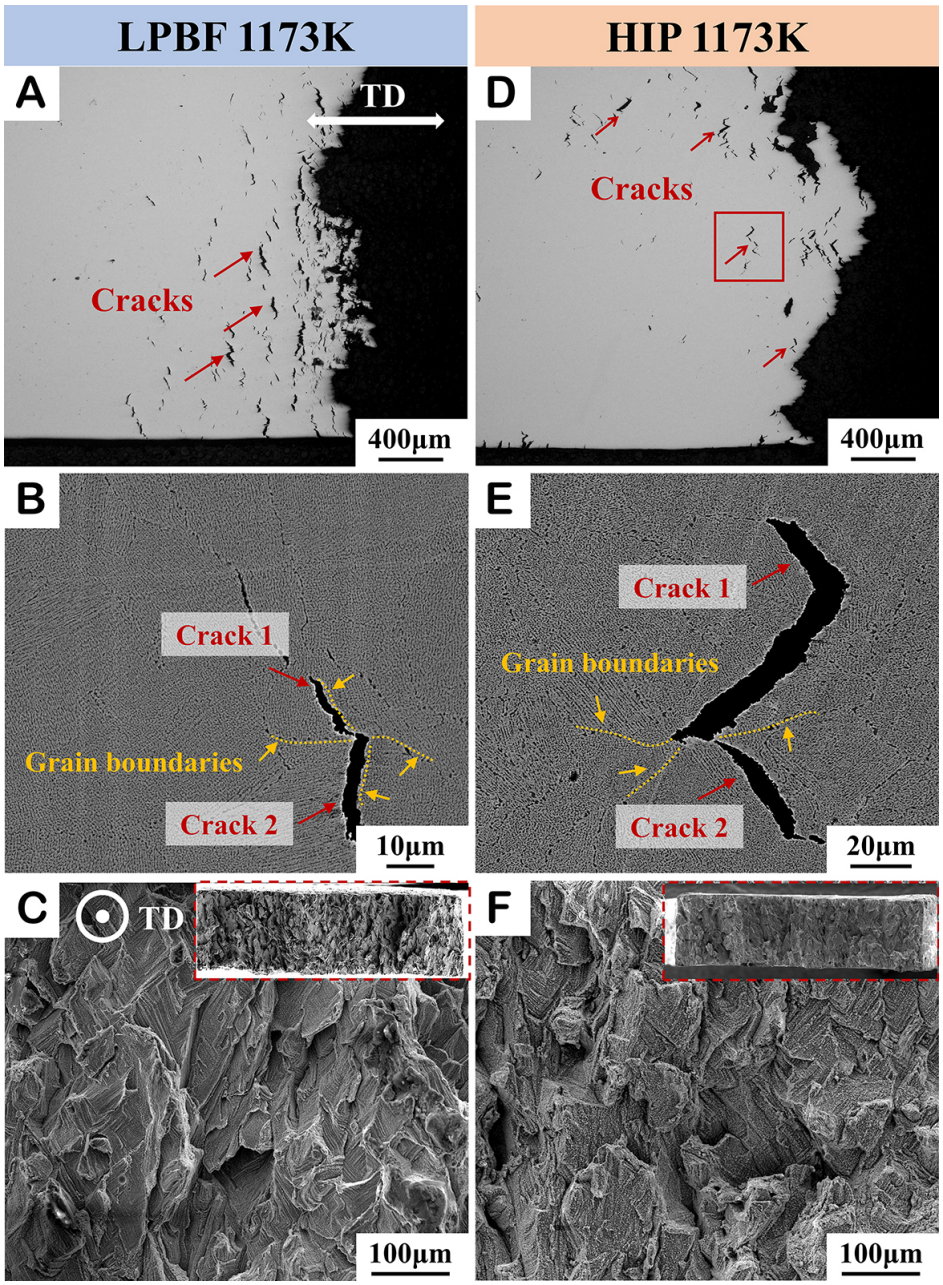

Figure 12. Fracture morphologies of Ni-Fe-Cr-Al-V HEAs at 1,173 K: (A-C) LPBF-processed and (D-F) HIP-processed.

can also contribute to the stability of the dislocation networks[18]. Figure 14 shows the TEM images of dislocation substructures in LPBF-processed HEA to illustrate the misorientation between substructures. The SAED patterns in [011] zone axes corresponding to areas I and II show that the misorientation between the two areas was calculated to be ~1°, indicating the extremely low misorientation. In our LPBF-processed HEAs, even at ultra-high stress levels, the good stability of pre-existing dislocation substructures is crucial for improving ductility. On the other hand, the dislocation shearing of the ordered $L1_2$ nanophases can lead to the predominant planar dislocation slip. Shearing of the ordered $L1_2$ precipitates by the first dislocation is expected to destroy the ordering and reduce the barrier of subsequent dislocation propagation on the same glide plane, leading to the "glide plane softening" and dislocation plane slip[43]. The combination of

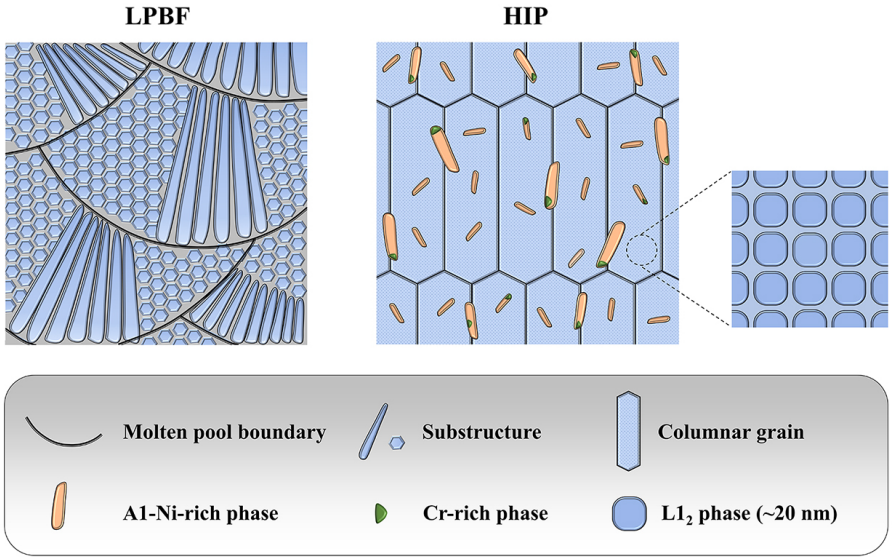

Figure 13. Schematic of microstructural evolution during HIP process.

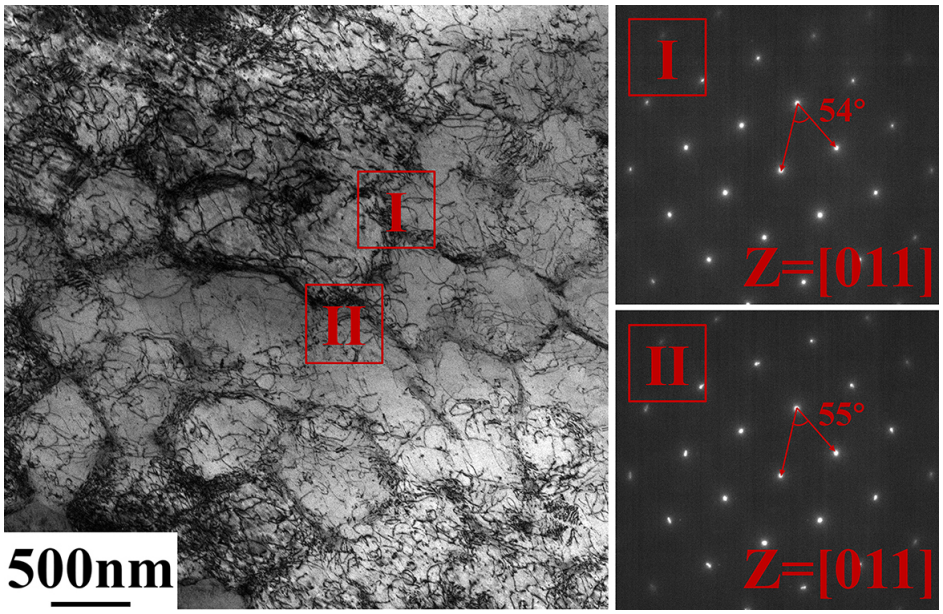

Figure 14. Misorientation between dislocation substructures in LPBF-processed HEA: BF image of dislocation substructures and SAED patterns in [011] zone axes corresponding to areas I and II, respectively.

dislocation substructure and $L1_2$ nanophase plays a significant role in obtaining favorable tensile properties of LPBF-processed HEA.

The initial microstructural features of Ni-Fe-Cr-Al-V HEA in LPBF and HIP states differ based on the microstructural analysis. After HIP treatment, B2 phases were precipitated at grain boundaries and grain interior, and the $L1_2$ phase grew up to 20 μm. Compared with the LPBF-processed HEA, the HIP-processed HEAs exhibited higher tensile strength at 773 K, but the ductility decreased slightly, which can be attributed to the existence of discontinuous B2 phase and continuous $L1_2$ phase. Conventionally, precipitation

strengthening is controlled by dislocation shearing or the dislocation bypass mechanisms (Orowan-type). In the HIP-processed HEAs, the precipitation strengthening contribution ($\Delta\sigma_{PPT}$) comes from the B2 phase and $L1_2$ nanophase. According to practice, the interaction between dislocations and the hard B2 phase can be interpreted by the Orowan bypass mechanism, while the $L1_2$ nanophase plays a role mainly through the dislocation shear mechanism. It is worth noting that the inhomogeneous deformation (i.e., strain gradient) caused by microstructure heterogeneity produces microscale residual stress and associated back stress, which may provide additional strengthening and strain hardening[39]. During the tensile deformation process, the plastic deformation is first borne by the softer FCC phase, resulting in dislocation accumulation and back stress strengthening at the heterogeneous interface between the FCC and B2 phases, which is why the alloy exhibits high strength characteristics[41]. In addition, the B2 phase gradually undergoes plastic deformation with the increase of tensile deformation. However, there is a strain gradient between the B2 phase and the FCC phases, and this strain gradient will stimulate heterogeneous deformation-induced strain hardening, which improves the work-hardening capacity of the material[44]. Figure 15 shows the schematic diagram of room-temperature deformation mechanism.

High temperature

As shown in Figure 9, the tensile strength of HIP-processed HEAs decreases while the ductility increases when tested at high temperatures (773 and 1,173 K). It is well known that relative sliding and migration of adjacent grains will occur under the drive of shear stresses at high temperatures. With the deformation temperature increasing from 733 to 1,173 K, the softening of HEA increased continuously. As mentioned above, the ET of the HEA is ~953 K, and the deformation mechanism will transform from intragranular dislocation slip to grain boundary sliding from the temperature lower than the ET to the temperature higher than ET. The dislocation substructures formed at grain interior could contribute to the strength improvement in LPBF-processed alloys at room temperature, and the stability of the substructure could be another factor maintaining the strength at 773 K. At 773 K, more active atomic motion and increasing slip system made the dislocation slip, climbing or cross-slip easier, and weaken the grain boundary hindrance. However, the plastic deformation mechanism of the HEAs at 773 K is still dominated by the intragranular dislocation slip. Therefore, the flow stress is only slightly decreased. At 1,173 K, the grain boundary strength diminishes, dropping below the intragranular strength, so the grain boundary sliding becomes easier and the deformation resistance (flow stress) is significantly reduced. In particular, the grain boundary sliding emerges as the dominant deformation mechanism. Figure 16 shows the schematic diagram of high-temperature deformation mechanism.

CONCLUSION

This study investigated the microstructural evolution and mechanical properties at room and high temperatures in LPBF-processed Ni-Fe-Cr-Al-V HEA. The main conclusions are as follows:

(1) The microstructure of LPBF-processed HEA contains dislocation substructure and FCC + $L1_2$ coherent structures. The dislocation substructure enabled the transmission of dislocations through the dislocation walls with the increase of stress and stabilized the plastic flow. The highly coherent FCC-$L1_2$ interfaces minimized the strain accumulation due to the dislocation shear and delayed the crack initiation. Consequently, the LPBF-processed HEA exhibits the desired strength-ductility combination (UTS: 1,088 MPa, FE: 29.4%).

(2) HIP treatment induced the microstructural evolution of HEA including the annihilation of the dislocation substructure, the growth of the $L1_2$ phase and the precipitation of the B2 phase. The precipitation of $L1_2$ and B2 phases could be ascribed to the precipitation modes dominated by CP and DP,

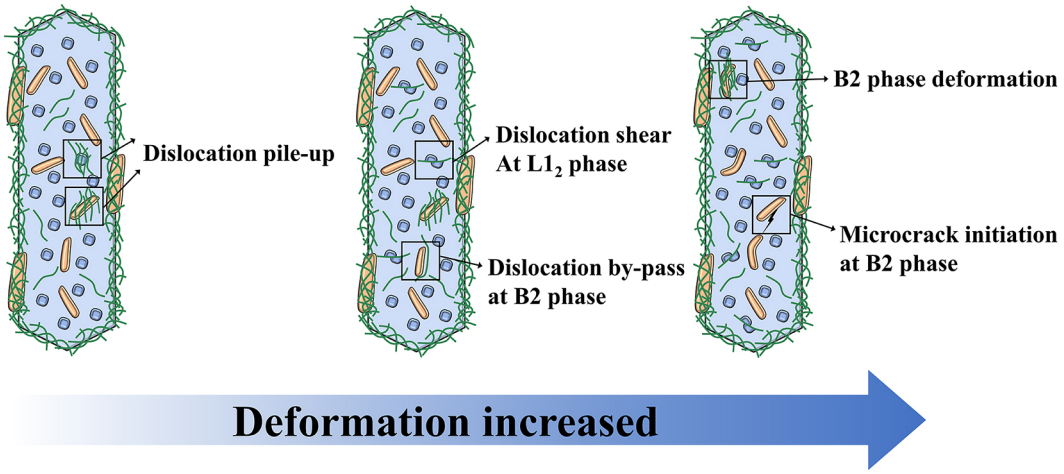

Figure 15. Schematic diagram of room-temperature deformation mechanism.

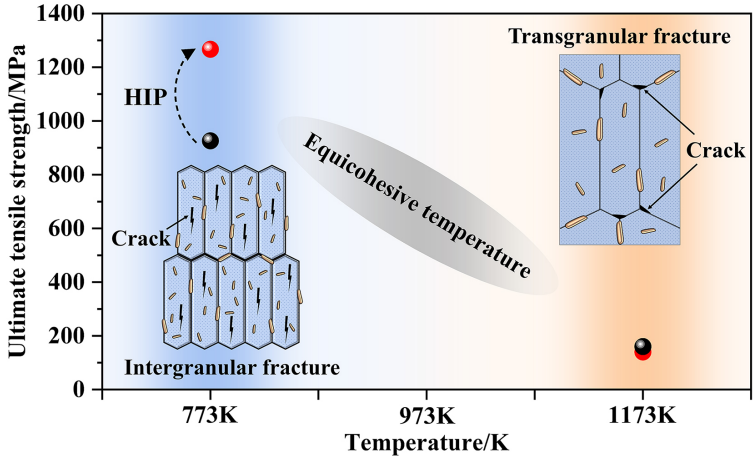

Figure 16. Schematic diagram of high-temperature deformation mechanism.

respectively. The tensile strength of the HEA after HIP increases to 1,334 MPa at room temperature, which could be mainly attributed to precipitation strengthening.

(3) With the deformation temperature increasing from 733 to 1,173 K, the softening of HEA increased continuously. However, intragranular dislocation slip is dominant at 773 K; more active atomic motion and increasing slip system of HEA make the dislocation slip, climbing or cross-slip easier, and weaken the grain boundary hindrance; thus, the strength decreases, while the residual dislocation substructures could reduce the strength decreasing. The grain boundary strength becomes lower than the intragranular strength at 1,173 K, and the grain boundary sliding becomes dominant; the deformation resistance is substantially reduced, resulting in significant softening of the HEA at this temperature.

DECLARATIONS

Authors' contributions

Conceptualization, visualization, formal analysis, writing - original draft, writing - review & editing: Liu Z

Conceptualization, methodology, writing - review & editing, funding acquisition, project administration: Tan Z
Supervision, writing - review & editing: Ma L
Methodology, funding acquisition: He D
Methodology: Zhou Z, Cui L
Supervision: Shao W, Guo X, Xue Y

Availability of data and materials
The data that support the findings of this study are available from the corresponding author upon reasonable request.

Financial support and sponsorship
This work is supported by the National Natural Science Foundation of China (Grant No. 51901004, No. 521771060, and No. 52001025). The present work also thanks the ZhongNuo Advanced Material (Beijing) Technology Co., Ltd, which provides initial materials for BMG amorphous powder and Zhongke Baice Technical Services Co. LTD for help in characterizing TEM observation.

Conflicts of interest
All authors declared that there are no conflicts of interest.

Ethical approval and consent to participate
Not applicable.

Consent for publication
Not applicable.

REFERENCES
1. Yeh JW, Chen SK, Lin SJ, et al. Nanostructured high-entropy alloys with multiple principal elements: novel alloy design concepts and outcomes. *Adv Eng Mater* 2004;6:299-303. DOI
2. Cantor B, Chang ITH, Knight P, Vincent AJB. Microstructural development in equiatomic multicomponent alloys. *Mater Sci Eng A* 2004;375-7:213-8. DOI
3. Kotadia HR, Gibbons G, Das A, Howes PD. A review of laser powder bed fusion additive manufacturing of aluminium alloys: microstructure and properties. *Addit Manuf* 2021;46:102155. DOI
4. Mu Y, He L, Deng S, et al. A high-entropy alloy with dislocation-precipitate skeleton for ultrastrength and ductility. *Acta Mater* 2022;232:117975. DOI
5. He ZF, Jia N, Ma D, Yan HL, Li ZM, Raabe D. Joint contribution of transformation and twinning to the high strength-ductility combination of a FeMnCoCr high entropy alloy at cryogenic temperatures. *Mater Sci Eng A* 2019;759:437-47. DOI
6. Pang J, Zhang H, Zhang L, et al. A ductile $Nb_{40}Ti_{25}Al_{15}V_{10}Ta_5Hf_3W_2$ refractory high entropy alloy with high specific strength for high-temperature applications. *Mater Sci Eng A* 2022;831:142290. DOI
7. Cui P, Bao Z, Liu Y, et al. Corrosion behavior and mechanism of dual phase $Fe_{1.125}Ni_{1.06}$CrAl high entropy alloy. *Corros Sci* 2022;201:110276. DOI
8. Yan Y, Mcgarrity KA, Delia DJ, Fekety C, Wang K. The oxidation-resistance mechanism of WTaNbTiAl refractory high entropy alloy. *Corros Sci* 2022;204:110377. DOI
9. Liu K, Nene SS, Frank M, Sinha S, Mishra RS. Extremely high fatigue resistance in an ultrafine grained high entropy alloy. *Appl Mater Today* 2019;15:525-30. DOI
10. Chen J, Zhou X, Wang W, et al. A review on fundamental of high entropy alloys with promising high-temperature properties. *J Alloys Compd* 2018;760:15-30. DOI
11. Yurchenko NY, Stepanov ND, Shaysultanov DG, Tikhonovsky MA, Salishchev GA. Effect of Al content on structure and mechanical properties of the Al_xCrNbTiVZr (x=0; 0.25; 0.5; 1) high-entropy alloys. *Mater Charact* 2016;121:125-34. DOI

12. Tsao TK, Yeh AC, Kuo CM, Murakami H. On the superior high temperature hardness of precipitation strengthened high entropy Ni-based alloys. *Adv Eng Mater* 2017;19:1600475. DOI
13. Bała P, Gorecki K, Bednarczyk W, Wątroba M, Lech S, Kawałko J. Effect of high-temperature exposure on the microstructure and mechanical properties of the $Al_5Ti_5Co_{35}Ni_{35}Fe_{20}$ high-entropy alloy. *J Mater Res Technol* 2020;9:551-9. DOI
14. Rivera-Díaz-del-Castillo PEJ, Fu H. Strengthening mechanisms in high-entropy alloys: perspectives for alloy design. *J Mater Res* 2018;33:2970-82. DOI
15. Zhang W, Chabok A, Kooi BJ, Pei Y. Additive manufactured high entropy alloys: a review of the microstructure and properties. *Mater Des* 2022;220:110875. DOI
16. Lin WC, Chang YJ, Hsu TH, et al. Microstructure and tensile property of a precipitation strengthened high entropy alloy processed by selective laser melting and post heat treatment. *Addit Manuf* 2020;36:101161. DOI
17. Yao H, Tan Z, He D, et al. High strength and ductility AlCrFeNiV high entropy alloy with hierarchically heterogeneous microstructure prepared by selective laser melting. *J Alloys Compd* 2020;813:152196. DOI
18. Liu L, Ding Q, Zhong Y, et al. Dislocation network in additive manufactured steel breaks strength-ductility trade-off. *Mater Today* 2018;21:354-61. DOI
19. Tascioglu E, Karabulut Y, Kaynak Y. Influence of heat treatment temperature on the microstructural, mechanical, and wear behavior of 316L stainless steel fabricated by laser powder bed additive manufacturing. *Int J Adv Manuf Technol* 2020;107:1947-56. DOI
20. Saeidi K, Gao X, Lofaj F, Kvetková L, Shen ZJ. Transformation of austenite to duplex austenite-ferrite assembly in annealed stainless steel 316L consolidated by laser melting. *J Alloys Compd* 2015;633:463-9. DOI
21. Sun S, Teng Q, Xie Y, et al. Two-step heat treatment for laser powder bed fusion of a nickel-based superalloy with simultaneously enhanced tensile strength and ductility. *Addit Manuf* 2021;46:102168. DOI
22. du Plessis A, Macdonald E. Hot isostatic pressing in metal additive manufacturing: X-ray tomography reveals details of pore closure. *Addit Manuf* 2020;34:101191. DOI
23. Shi Q, Qin F, Li K, Liu X, Zhou G. Effect of hot isostatic pressing on the microstructure and mechanical properties of 17-4PH stainless steel parts fabricated by selective laser melting. *Mater Sci Eng A* 2021;810:141035. DOI
24. Rezaei A, Kermanpur A, Rezaeian A, et al. Contribution of hot isostatic pressing on densification, microstructure evolution, and mechanical anisotropy of additively manufactured IN718 Ni-based superalloy. *Mater Sci Eng A* 2021;823:141721. DOI
25. Liang YJ, Wang L, Wen Y, et al. High-content ductile coherent nanoprecipitates achieve ultrastrong high-entropy alloys. *Nat Commun* 2018;9:4063. DOI PubMed PMC
26. Wang L, Wang L, Zhou S, et al. Precipitation and micromechanical behavior of the coherent ordered nanoprecipitation strengthened Al-Cr-Fe-Ni-V high entropy alloy. *Acta Mater* 2021;216:117121. DOI
27. Gawel R, Rogal Ł, Grzesik Z. Behaviour of Al, Co, Cr, Ni-based high entropy alloys under high-temperature thermal shock oxidising conditions. *Corros Sci* 2022;198:110116. DOI
28. Kong D, Dong C, Wei S, et al. About metastable cellular structure in additively manufactured austenitic stainless steels. *Addit Manuf* 2021;38:101804. DOI
29. Zhu ZG, Nguyen QB, Ng FL, et al. Hierarchical microstructure and strengthening mechanisms of a CoCrFeNiMn high entropy alloy additively manufactured by selective laser melting. *Scr Mater* 2018;154:20-4. DOI
30. Jin M, Piglione A, Dovgyy B, et al. Cyclic plasticity and fatigue damage of CrMnFeCoNi high entropy alloy fabricated by laser powder-bed fusion. *Addit Manuf* 2020;36:101584. DOI
31. Liu Z, Tan Z, He D, et al. Simultaneously improved the strength and ductility of laser powder bed fused Al-Cr-Fe-Ni-V high-entropy alloy by hot isostatic pressing: microcrack closure and precipitation strengthening. *J Mater Sci Technol* 2024;180:55-68. DOI
32. Spierings AB, Schneider M, Eggenberger R. Comparison of density measurement techniques for additive manufactured metallic parts. *Rapid Prototyp J* 2011;17:380-6. DOI
33. Schneider CA, Rasband WS, Eliceiri KW. NIH image to imageJ: 25 years of image analysis. *Nat Methods* 2012;9:671-5. DOI PubMed PMC
34. Dai Y, Kong QP. On the physical origin of equicohesive temperature for creep. *Strength Metals Alloys* 1989;2:959-64. DOI
35. Wang K, Jin X, Jiao ZM, Qiao JW. Mechanical behaviors and deformation constitutive equations of CrFeNi medium-entropy alloys under tensile conditions from 77 K to 1073 K. *Acta Metall Sin* 2022;59:277-88. DOI
36. Li W, Ma L, Peng P, et al. Microstructural evolution and deformation behavior of fiber laser welded QP980 steel joint. *Mater Sci Eng A* 2018;717:124-33. DOI
37. Liu Z, Zhao D, Wang P, et al. Additive manufacturing of metals: microstructure evolution and multistage control. *J Mater Sci Technol* 2022;100:224-36. DOI
38. Zhao D, Guo Y, Lai R, et al. Abnormal three-stage plastic deformation in a 17-4 PH stainless steel fabricated by laser powder bed fusion. *Mater Sci Eng A* 2022;858:144160. DOI
39. Zhang H, Li C, Yao G, Shi Y, Zhang Y. Effect of annealing treatment on microstructure evolution and deformation behavior of 304 L stainless steel made by laser powder bed fusion. *Int J Plasticity* 2022;155:103335. DOI
40. Vilanova M, Garciandia F, Sainz S, Jorge-badiola D, Guraya T, San Sebastian M. The limit of hot isostatic pressing for healing cracks present in an additively manufactured nickel superalloy. *J Mater Proc Technol* 2022;300:117398. DOI
41. Liu Z, Tan Z, Yao H, et al. Heat treatment induced microstructural evolution and strength enhancement of Al-Cr-Fe-Ni-V high-entropy alloy fabricated by laser powder bed fusion. *Mater Sci Eng A* 2022;861:144348. DOI

42. Fang JYC, Liu WH, Luan JH, Yang T, Fu MW, Jiao ZB. Dual effects of pre-strain on continuous and discontinuous precipitation of L12-strengthened high-entropy alloys. *J Alloys Compd* 2022;925:166730. DOI
43. Wei LL, Gao GH, Kim J, Misra RDK, Yang CG, Jin XJ. Ultrahigh strength-high ductility 1 GPa low density austenitic steel with ordered precipitation strengthening phase and dynamic slip band refinement. *Mater Sci Eng A* 2022;838:142829. DOI
44. Shi P, Zhong Y, Li Y, et al. Multistage work hardening assisted by multi-type twinning in ultrafine-grained heterostructural eutectic high-entropy alloys. *Mater Today* 2020;41:62-71. DOI